Supplemental Material for "Emergent Elasticity in Amorphous Solids"

Jishnu N. Nampoothiri,[1,2] Yinqiao Wang,[3] Kabir Ramola,[2]
Jie Zhang,[3] Subhro Bhattacharjee,[4] and Bulbul Chakraborty[1]

[1] *Martin Fisher School of Physics, Brandeis University, Waltham, MA 02454 USA*
[2] *Centre for Interdisciplinary Sciences, Tata Institute of Fundamental Research, Hyderabad 500107, India*
[3] *Institute of Natural Sciences and School of Physics and Astronomy, Shanghai Jiao Tong University, Shanghai, 200240 China*
[4] *International Centre for Theoretical Sciences, Tata Institute of Fundamental Research, Bengaluru 560089, India*

In this supplementary document, we describe in detail several key aspects of the theoretical framework and analysis of numerical and experimental data. In Section 1, we describe the methods used to generate the data used in this letter. In Section 2, we outline the derivation of the Gauss's law constraint on the Cauchy Stress tensor starting from the constraints of force and torque balance on every grain and discuss the mapping of grain-level properties to the continuum theory. In Section 3, we present results for the correlations of the electric displacement tensor $\hat{D}$, in a polarizable medium characterized by $\hat{\Lambda}$. Further in Section 4, we present experimental data for stress correlations from individual configurations. Finally, Section 5 describes the numerical results for the 2D system at finite temperature.

S1. METHODS

The main quantity of interest in this study, for a given packing is the stress tensor field in Fourier space given by

$$\hat{\sigma}^p(\mathbf{q}) = \sum_{g=1}^{N_G^p} \hat{\sigma}_g^p \exp\left(i\mathbf{q}\cdot\mathbf{r}_g^p\right). \tag{S1}$$

Here, 'p' denotes a particular realization or packing of N_G^p grains, while g denotes a particular grain in the packing located at $\mathbf{r}_g^p$. $\hat{\sigma}_g^p$ represents the force moment tensor for the grain g, given by

$$\hat{\sigma}_g^p = \sum_{c=1}^{n_c^g} \mathbf{r}_c^g \otimes \mathbf{f}_c^g. \tag{S2}$$

Here $\mathbf{r}_c^g$ denotes the position of the contact c from the center of the grain g and $\mathbf{f}_c^g$ denotes the inter-particle force at the contact.

S1.1. Numerical Methods

We generate jammed packings of frictionless spheres interacting through one-sided spring potentials in two and three dimensions. Our implementation follows the standard O'Hern protocol [1–3], with energy minimization performed using two procedures (i) conjugate gradient minimization, and (ii) a FIRE [4, 5] minimization implementation in LAMMPS [6]. We have verified that these differences in protocol do not modify our results.

We simulate a 50:50 mixture of grains with diameter ratio 1:1.4. In our simulations, the system lengths are held fixed at $L_x = L_y = 1$ in 2D and $L_x = L_y = L_z = 1$ in 3D. We impose periodic boundary conditions in each direction, setting a lower cutoff between points in Fourier space $q_{min} = 2\pi$. We choose an upper cutoff $q_{max} = \pi/d_{min}$ so as to not consider stress fluctuations occurring at length scales shorter than d_{min}, the diameter of the smallest grain in the packing. We have presented data for system sizes $N = 512, 1024, 2048, 4096, 8192$ in 2D, averaged over atleast 100 configurations for each system size. The results obtained for different system sizes have been collapsed (see Fig. 1 of the main text) using the system size N and q_{max} as scaling parameters. This shows that the data presented is not significantly affected by finite size effects. All the 2D packings have a pressure per grain $P \in [0.016, 0.017]$ and packing fraction $\phi \in [0.878, 0.882]$. In 3D, the data for $N = 27000$ is presented in Fig. 2 of the main text, the data have been averaged over 350 configurations. The range of packing fractions for these configurations is $\phi \in [0.686, 0.689]$, with a pressure per grain $P \in [0.0136, 0.0147]$.

S1.2. Experimental Methods

The experimental results were produced from the analyses of isotropically jammed packings and pure-sheared packings, which were both prepared using a biaxial apparatus whose details can be found in Wang Et al. 2018 [7]. This apparatus mainly consists of a rectangular frame mounted on top of a powder-lubricated horizontal glass plate. Each pair of parallel walls of the rectangular frame can move symmetrically with a motion precision of 0.1 mm so that the center of mass of the frame remains fixed. To apply isotropic compression, the two pairs of walls are programed to move inwards symmetrically. To apply pure shear, one pair of walls moves inwards, and the other pair of walls moves outwards, such that the area of the rectangle is kept fixed. The motion of walls is sufficiently slow to guarantee that the deformation is quasi-static. About 1.5 m above the apparatus, there is an array of 2×2 high-resolution (100 pixel/cm) cameras that are aligned and synchronized.

To prepare an isotropically jammed packing, we first filled the rectangular area with a 50:50 mixture of 2680 bi-dispersed photoelastic disks (Vishay PSM-4), with diameters of 1.4 cm and 1.0 cm, to create the various unjammed random initial configurations. Next, we applied isotropic compression to the disks to achieve a definite packing fraction ϕ, which is the ratio between the area of disks and that of the rectangle. To minimize the potential inhomogeneity of force chains in the jammed packing, we constantly applied mechanical vibrations before the ϕ exceeded the jamming point $\phi_J \approx 84.0\%$ of frictionless particles. The final isotropically jammed packing is confined in a square domain of 67.2 cm × 67.2 cm. Here, $\phi \approx 84.4\%$, the mean coordination number is around 4.1, the pressure is around 12 N/m, and the corresponding dimensionless pressure is 2×10^{-4}. Once the isotropically jammed packing was prepared, we then applied pure shear of strain 1.5% to the packing to produce the pure-sheared packing. For both types of packings, two different images were recorded. Disk positions were obtained using the *normal image*, recorded without polarizers. Contact forces were analyzed from the *force-chain image*, recorded with polarizers, using the force-inverse algorithm [8].

S2. MAPPING OF GRANULAR MEDIA TO CONTINUUM VECTOR CHARGE TENSOR GAUGE THEORY

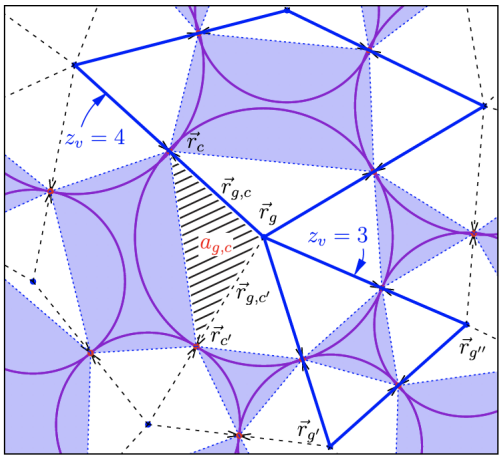

FIG. S1: A section of a jammed configuration of soft frictionless disks in 2D. The centers of the grains are located at positions $\mathbf{r}_g$. The contact points between grains are located at positions $\mathbf{r}_c$. The triangle formed by the points $\mathbf{r}_g, \mathbf{r}_{g'}, \mathbf{r}_c$ (shaded area) is uniquely assigned to the contact c and has an associated area $a_{g,c}$.

The VCT Gauss's law (Eq. (2) in the main text), is widely accepted as the coarse-grained description of stresses in athermal solids in mechanical equilibrium [9, 10]. Here, we demonstrate the emergence of this Gauss's law from local constraints of mechanical equilibrium, for the specific example of disordered granular solids. The arguments can be easily generalized to other amorphous packings at zero temperature. Granular materials consist of an assembly of grains that interact with each other via contact forces, as shown in Fig. S1. In a granular solid, each grain is in mechanical equilibrium and thus, satisfy the constraints of force and torque balance. The constraints of force and

torque balance on a grain g, with no "body forces" can be written as:

$$\begin{aligned} \sum_{c\in g} \mathbf{f}_{g,c} &= 0, \\ \sum_{c\in g} \mathbf{r}_{g,c} \times \mathbf{f}_{g,c} &= 0 \ , \end{aligned} \tag{S3}$$

respectively. Here, $\mathbf{f}_{g,c}$ is the contact force, and $\mathbf{r}_{g,c}$ the vector joining the center of grain g to the contact c (Fig. S1). This places $dN + d(d-1)N$ nontrivial constraints on the N grains that are part of the contact network. A grain is said to be a part of the contact network if it has more than one contact and grains which are not part of the contact network are defined to be "rattlers". In our representation, the rattlers become part of voids. Given a set of $\mathbf{f}_{g,c}$ and $\mathbf{r}_{g,c}$, one can define a stress tensor for a grain with area A_g:

$$\hat{\sigma}_g = (1/A_g) \sum_{c\in g} \mathbf{r}_{g,c} \otimes \mathbf{f}_{g,c} \ . \tag{S4}$$

The coarse-grained stress tensor field, $\hat{D}(\mathbf{r})$ is obtained by summing $\hat{\sigma}_g$ over all grains included in a coarse-graining volume, Ω_r, centered at $\mathbf{r}$:

$$\hat{D}(\mathbf{r}) = \frac{1}{\Omega_r} \sum_{g\in\Omega_r} A_g \hat{\sigma}_g \ . \tag{S5}$$

The symmetry of $\hat{\sigma}_g$ is easy to establish by writing every contact force as the sum of a normal force, which is along the contact vector $\mathbf{r}_{g,c}$, and a tangential force perpendicular to it. The normal part leads to a symmetric contribution to $\hat{\sigma}_g$. Using the torque-balance equation, Eq. (S3), the contribution from the tangential forces sum up to zero. To establish the divergence free condition, we follow the approach outlined in Degiuli, E. and McElwaine, J. 2011 [11] by first subdividing $\hat{\sigma}_g$ into contributions from each contact. As seen from Fig. S1, we can associate a triangle of area $a_{g,c}$ with each contact, and $A_g = \sum_{c\in g} a_{g,c}$. Adopting a convention that we traverse around a grain in a counterclockwise direction, we associate with contact c, the triangle that is defined by c and the contact c' that follows it. We can then write: $A_g\hat{\sigma}_g = \sum_{c\in g} a_{g,c}\hat{\sigma}_c$, where $\hat{\sigma}_c$ is yet to be defined. Comparing to Eq. (S4), we see that $a_{g,c}\hat{\sigma}_c = \mathbf{r}_{g,c} \otimes \mathbf{f}_{g,c}$, therefore $\hat{\sigma}_c = \mathbf{r}_{g,c} \otimes \mathbf{f}_{g,c}/a_{g,c}$. The signed area $a_{g,c}$ is given by $a_{g,c} = (1/2)\mathbf{r}_{g,c} \times (\mathbf{r}_{c'} - \mathbf{r}_c)$. The divergence theorem is: $\int_V \partial_i\sigma_{ij} = \int_{\partial V} n_i\sigma_{ij}$, where $\hat{n}$ is the unit normal to ∂V, which can be written as as $\int_V \nabla\cdot\hat{\sigma} = \int_{\partial V}(d\mathbf{r}\times\hat{\sigma})_j$. We can apply the discrete version of this theorem to $\hat{\sigma}_g$ to get:

$$A_g(\nabla\cdot\hat{\sigma})_g = \sum_{c\in g} \hat{\sigma}_c \times (\mathbf{r}_{c'} - \mathbf{r}_c) = \sum_{c\in g} \mathbf{f}_{g,c} = \mathbf{f}_{ext} \ . \tag{S6}$$

In the absence of external forces, $\hat{\sigma}_g$ is divergence free. This grain-level condition leads to a similar condition on $\hat{D}(\mathbf{r})$: $\Omega_r\nabla\cdot\hat{D}(\mathbf{r}) = \sum_{c\in\partial\Omega} \mathbf{f}_c$, where the sum is over the contact forces on the boundary of Ω, which is still discrete.

To map to the continuum theory, we posit that disorder averaging over all discrete networks that occur under given external conditions leads to

$$\partial_i(\hat{D}(\mathbf{r}))_{ij} = (f_{ext})_j.$$

We expect this mapping to be accurate if the coarse-graining volume Ω is much larger than a typical grain volume. The excellent correspondence between disorder-averaged $\hat{D}$ correlations measured in granular packings and theoretical predictions, shown in the main text justifies the above mapping. In Section 3 of this Supplementary Information, we present experimental measurements of $\hat{D}$ correlations in *individual* configurations to show that self-averaging is a very good approximation for internal stresses in granular media.

S3. STRESS-STRESS CORRELATIONS IN POLARIZABLE MEDIA

In this section we present expressions for the correlations of the $\hat{D}$ tensor, analogous to the expressions for the $\hat{E}$ correlations in vacuum (Eq. (7) in the main text). The starting point is Eq. (5) in the main text: Gauss's law and the magnetostatic condition for a polarizable medium characterized by the rank-4 tensor, $\hat{\Lambda}$. In the vacuum

theory [12], the strategy is to project out the divergence mode from the completely isotropic rank-4 tensor, using the magnetostatic condition. This condition in **q**- space, for a polarizable medium is given by

$$D_{ij}(\mathbf{q}) = (\hat{\Lambda}^{-1}\hat{A})_{ij}(\boldsymbol{q}); \quad A_{ij}(\mathbf{q}) \equiv \mathbf{q} \otimes \boldsymbol{\phi} \ , \tag{S7}$$

where $\boldsymbol{\phi}$ is the electrostatic gauge potential, as discussed in the main text. Since $\hat{\Lambda}$ has to obey the symmetry $ij \to ji$, it is simpler to write the components of $\hat{D}$ as a vector of length 3 in 2D: (D_{xx}, D_{yy}, D_{xy}), and a vector of length 6 in 3D. The rank-4 tensor can be then expressed as a 3×3 (2D) and a 6×6 (3D) matrix [13]. Furthermore, if $\hat{\Lambda}$ is a symmetric matrix in this representation, then the $\hat{D} - \hat{D}$ correlations can be obtained from the $\hat{E} - \hat{E}$ correlations by a transformation of the metric: $\mathbf{q} \to \bar{\mathbf{q}}(\hat{\Lambda})$. Such a transformation is reminiscent of the emergence of birefringence in quantum spin ice in the presence of an applied electric field [14]. For the more general situation that can occur in granular media the matrix is not symmetric, and a cleaner approach is to use the dual formalism in which the potential is obtained by solving Gauss's law [15]. In this dual formalism, potentials in 2D and 3D appear differently: a scalar in 2D and a second-rank symmetric tensor in 3D. The expression for the correlations of the potentials can be worked out explicitly, and from that the $\hat{D} - \hat{D}$ correlations can be obtained in a straightforward manner. In 2D, $\partial_i D_{ij} = 0$ is solved by introducing a potential [15–19], ψ : $D_{ij} = \epsilon_{ia}\epsilon_{jb}\partial_a\partial_b\psi$. The potential in 3D is a symmetric tensor, ψ_{ij}: $D_{ij} = \epsilon_{iab}\epsilon_{jcd}\partial_a\partial_c\psi_{bd}$

Here, we present the explicit construction of the correlations of D_{ij} in 2D [16–18]. The magnetostatic condition implies that $\hat{\Lambda}$ acts as a stiffness tensor in a Gaussian theory. Using the $\boldsymbol{q}$-space representation: $D_{ij}(\mathbf{q}) = \epsilon_{ia}\epsilon_{jb}q_a q_b\psi(\mathbf{q})$, The correlations $\langle\psi(\mathbf{q})\psi(-\mathbf{q})\rangle$ can be computed, and give:

$$\begin{aligned} \langle\psi(\mathbf{q})\psi(-\mathbf{q})\rangle &= [A_{ij}(\mathbf{q})\Lambda_{ijkl}A_{kl}(-\mathbf{q})]^{-1}, \\ A_{ij} &= q^2\delta_{ij} - q_i q_j. \end{aligned} \tag{S8}$$

The correlations of D_{ij} then follow as:

$$\langle D_{ij}(\mathbf{q})D_{kl}(-\mathbf{q})\rangle = \epsilon_{ia}\epsilon_{jb}\epsilon_{kc}\epsilon_{ld}q_a q_b q_c q_d\langle\psi(\mathbf{q})\psi(-\mathbf{q})\rangle.$$

For the special case of $\hat{\Lambda}$ being a diagonal tensor with components λ_i, $i = xx\ , yy\ , xy$, the correlations simplify to:

$$\begin{aligned} C_{xxxx}(\mathbf{q}) &= \langle D_{xx}(\mathbf{q})\, D_{xx}(-\mathbf{q})\rangle = \frac{q_y^4}{\lambda_{xx}q_y^4 + \lambda_{yy}q_x^4 + 2\lambda_{xy}q_x^2q_y^2}, \\ C_{xyxy}(\mathbf{q}) &= \langle D_{xy}(\mathbf{q})\, D_{xy}(-\mathbf{q})\rangle = \frac{q_x^2q_y^2}{\lambda_{xx}q_y^4 + \lambda_{yy}q_x^4 + 2\lambda_{xy}q_x^2q_y^2}, \\ C_{yyyy}(\mathbf{q}) &= \langle D_{yy}(\mathbf{q})\, D_{yy}(-\mathbf{q})\rangle = \frac{q_x^4}{\lambda_{xx}q_y^4 + \lambda_{yy}q_x^4 + 2\lambda_{xy}q_x^2q_y^2}, \\ C_{xxxy}(\mathbf{q}) &= \langle D_{xx}(\mathbf{q})\, D_{xy}(-\mathbf{q})\rangle = -\frac{q_xq_y^3}{\lambda_{xx}q_y^4 + \lambda_{yy}q_x^4 + 2\lambda_{xy}q_x^2q_y^2}, \\ C_{xxyy}(\mathbf{q}) &= \langle D_{xx}(\mathbf{q})\, D_{yy}(-\mathbf{q})\rangle = \frac{q_x^2q_y^2}{\lambda_{xx}q_y^4 + \lambda_{yy}q_x^4 + 2\lambda_{xy}q_x^2q_y^2}, \\ C_{xyyy}(\mathbf{q}) &= \langle D_{xy}(\mathbf{q})\, D_{yy}(-\mathbf{q})\rangle = -\frac{q_yq_x^3}{\lambda_{xx}q_y^4 + \lambda_{yy}q_x^4 + 2\lambda_{xy}q_x^2q_y^2}. \end{aligned} \tag{S9}$$

The experimental and numerical measurements of correlations in 2D, shown in Fig. 1 of the main text and in Fig. S2 of the supplementary, have been fit to the above forms. To analyze the correlations in isotropically compressed 3D packings, we assume that $\hat{\Lambda}$ is the identity tensor and use Eq. (7) of the main text, which gives the correlations in vacuum with an overall stiffness constant, λ.

S4. FORCE CHAINS AND STRESS CORRELATIONS

A striking consequence of the anisotropic correlations in **q**-space is evident if we analyze the correlations of the normal stresses, D_{xx} and D_{yy} in real space. The Fourier Transform of C_{xxxx} in isotropic systems, with $\hat{\Lambda} = \lambda\mathbb{1}$

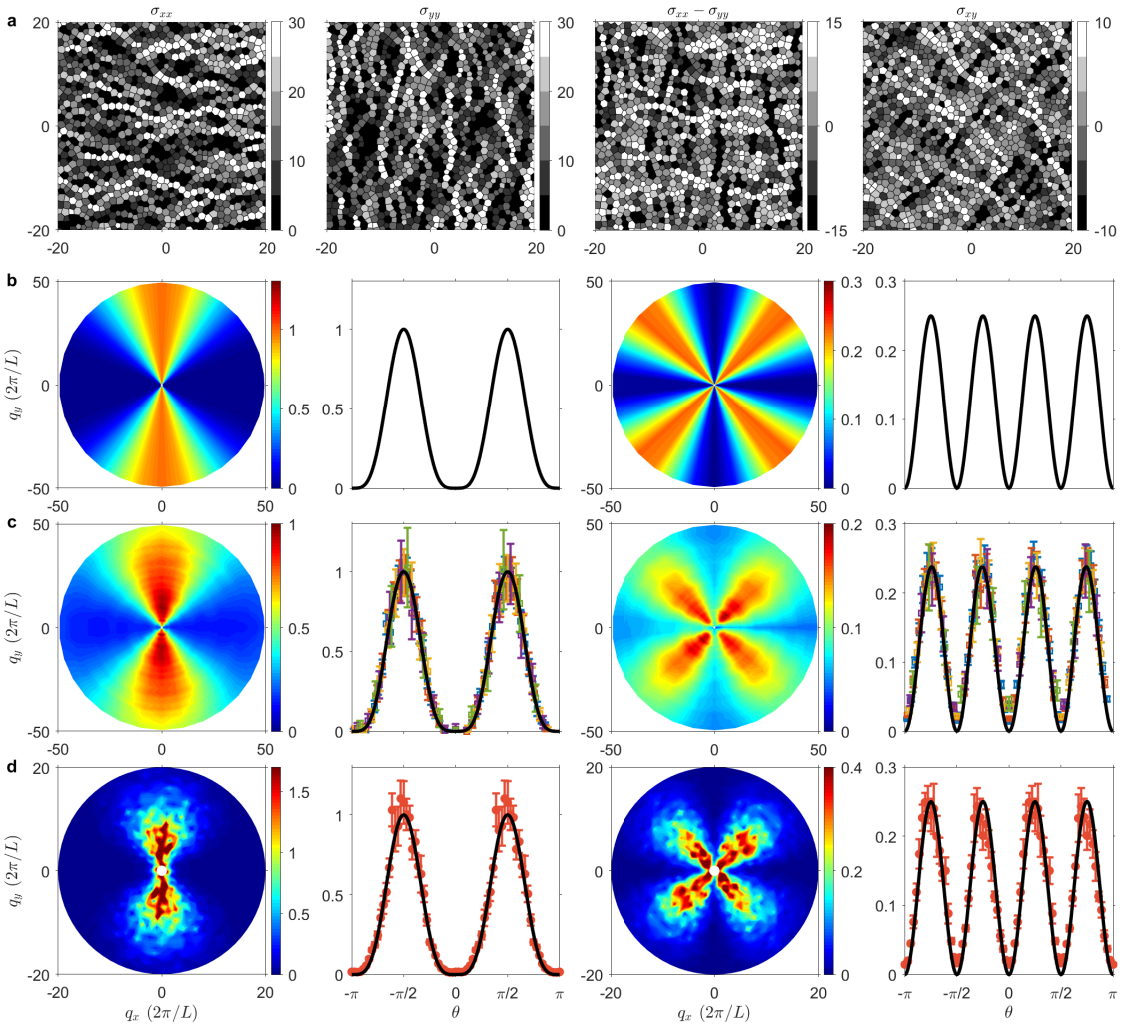

FIG. S2: **Comparisons in Fourier space between the theoretical predictions (black line) with $\Lambda = \mathbb{1}$, and the numerical and the experimental results (symbols) of the stress-stress correlations in 2D, isotropically jammed systems. a**, Photo-elastic images, in which each grain is shaded according to the magnitude of its normal stress, exhibit clear filamentary structures that are normally referred to as force chains. **b**, Theoretical predictions of $C_{xxxx}(q,\theta)$ and $C_{xyxy}(q,\theta)$, which are independent of q, and the corresponding angular functions $C_{xxxx}(\theta)$ and $C_{xyxy}(\theta)$. **c**, Numerical data of the frictionless jammed packings within the range of pressure $P \in [0.016, 0.017]$. The results of the five different system sizes $N = 512, 1024, 2048, 4096, 8192$ are shown in the angular plots. **d**, Experimental data from *frictional* packings within the range of pressure $P \in [1.5 \times 10^{-4}, 2.9 \times 10^{-4}]$. All correlation functions are normalized by their peak values of $C_{xxxx}(\theta)$. The units of q are $2\pi/L$, where L is the system size: $L \approx 100 d_{\min}$ in simulations, $L = 40 d_{\min}$ in experiments. Here $d_{\min}$ is the diameter of the small particle. Both the numerical and experimental data start to deviate from the theoretical predictions around $q \geq 2\pi/4d_{\min}$, indicating the breakdown of the continuum limit.

illustrates the point:

$$\begin{aligned} C_{xxxx}(r_x, r_y) &= \frac{3}{2\lambda r_x^2} \quad \text{for} \quad r_x \gg r_y, \\ C_{xxxx}(r_x, r_y) &= -\frac{1}{2\lambda r_y^2} \quad \text{for} \quad r_y \gg r_x. \end{aligned} \tag{S10}$$

The reverse is true for C_{yyyy}. The consequence of this feature is that the transverse correlations become *negatively* correlated. The photo-elastic images from 2D experiments, shown in the main text and in Figs. S3 and S4, are a striking visual representation of this stark difference between longitudinal and transverse correlations, which in turn is a manifestation of the conservation of "charge-angular-momentum", and the resulting sub-dimensional propagation [20].

The $U(1)$ gauge theory with vector charges, therefore, clarifies the meaning of force-chains within a continuum, disorder-averaged theory.

S4.1. Additional Analysis of Experiments

In this subsection, we present results of stress correlations from individual configurations in the sheared experimental packings to illustrate how well self-averaging works in these jammed packings. We note that our systems are deep in the jammed region: we do not address the possible breakdown of self-averaging close to the unjamming transition.

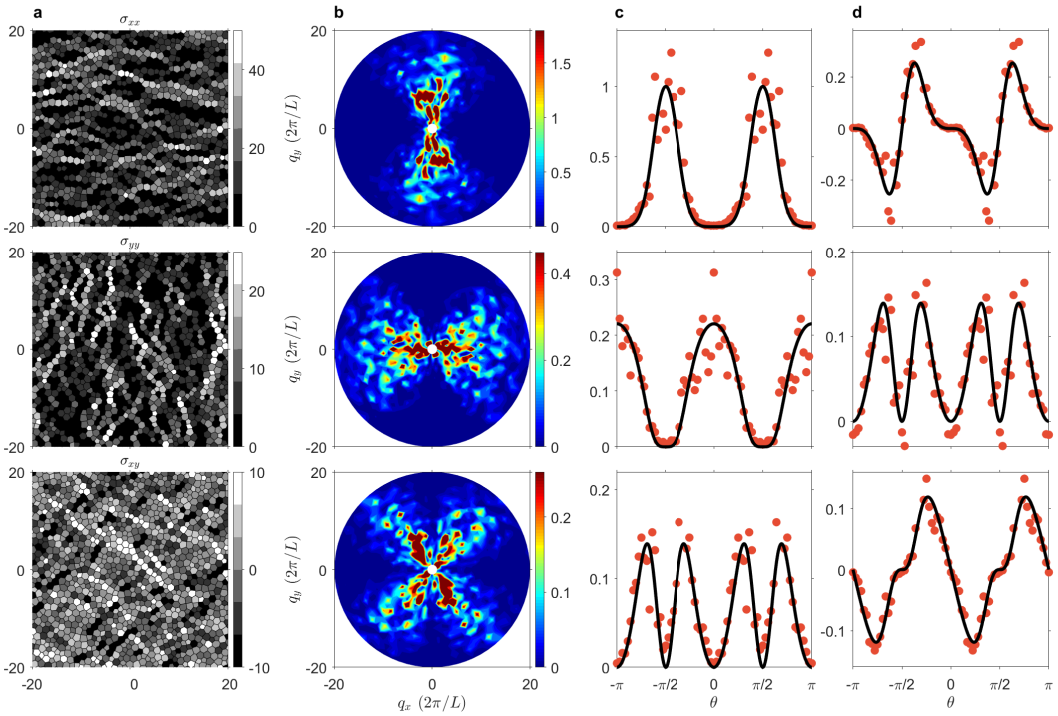

FIG. S3: Experimental measurements of correlations in Fourier space, for a single packing in the ensemble of packings, used to generate the *averaged* correlations shown in the main text (Fig. 3). The features observed in these averaged correlations, are seen to emerge in a single packing, demonstrating the self-averaging property of the stress in these packings that are deep in the jammed regime.

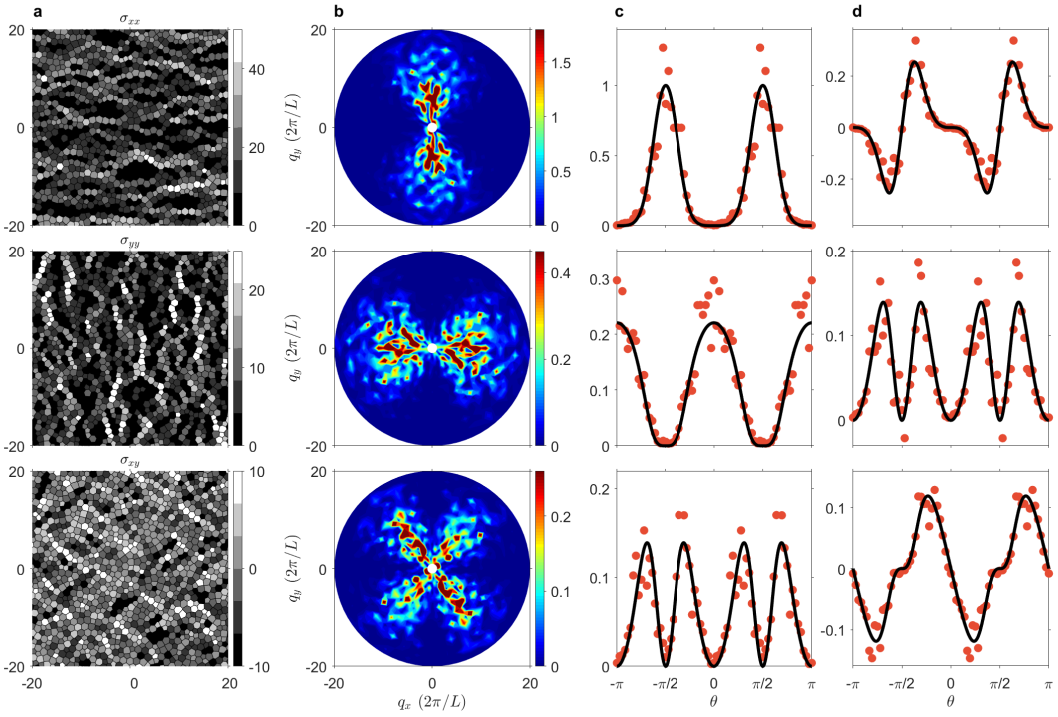

FIG. S4: Experimental measurements of correlations in Fourier space, for a second packing created under the same external conditions as in Fig. S3

S5. FINITE TEMPERATURE RESULTS

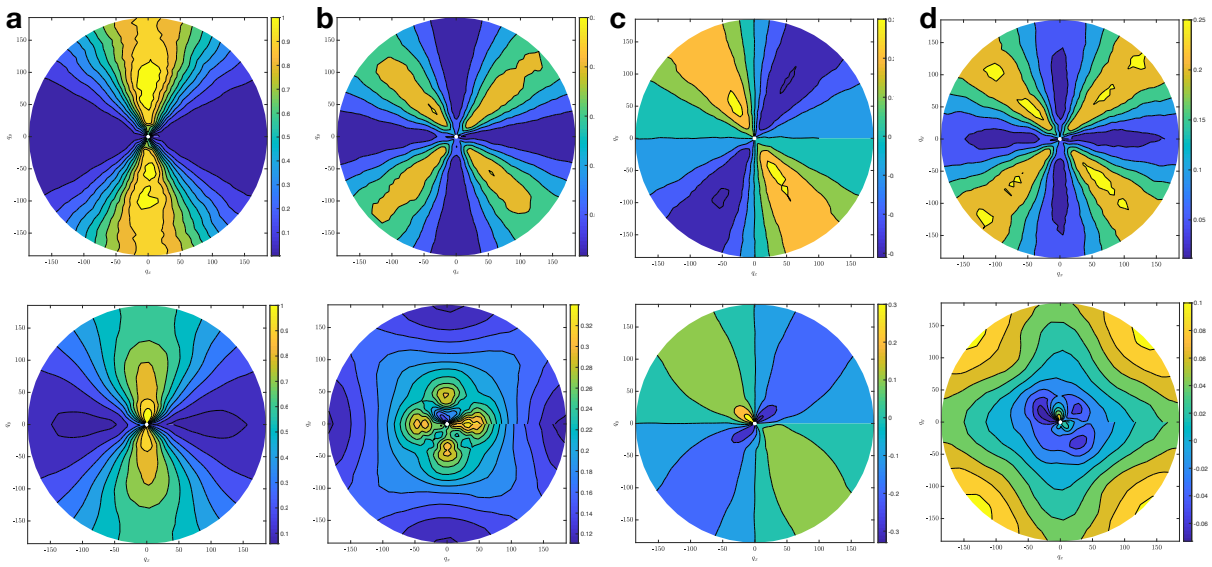

FIG. S5: Comparisons in Fourier space between stress correlations at zero (**Top**) and finite (**Bottom**) temperatures . The columns **a**, **b**, **c**, and **d** show the results for correlation functions C_{xxxx}, C_{xyxy}, C_{xxxy} and C_{xxyy} respectively. The packings used have an average compression energy per grain $E_{compression} \approx 10^{-4}$ and the finite temperature results have an average thermal energy per grain $E_{thermal} \approx 3.9 \times 10^{-4}$.

Pinch point singularities are one of the salient features of the VCT correlation functions. These singularities originate from the strict constraints of mechanical equilibrium imposed on athermal systems. For a system at finite

temperature however, these constraints can be violated and hence we expect the pinch point singularities to disappear at finite temperatures. Thus, the presence of a pinch point singularity is a hallmark of an athermal system. The numerically generated stress correlations from a 2D system at finite temperature is shown in Fig. S5 and it can be clearly seen that the pinch point singularity has vanished at this temperature ($E_{thermal}/E_{compression} = 3.9$).

The numerical simulations were carried out in LAMMPS and the finite temperature was imposed through a Nosé -Hoover thermostat. The protocol is to start with a valid athermal $T = 0$ configuration, generated following the procedure described in the Numerical Methods Section and then perform finite temperature dynamics to compute the stress correlations at a non-zero temperature. This procedure is then repeated over multiple initial athermal configurations and ensemble averaged to obtain the finite temperature stress correlations. The results displayed are obtained for packings of 8192 disks with an average pressure per grain $P \in [0.016, 0.017]$. The results shown have been averaged over 50 starting athermal configurations in 2D with 50 finite temperature configurations sampled during the finite temperature molecular dynamics run, for each of the 50 starting configurations.

[1] O'Hern, C. S., Langer, S. A., Liu, A. J. & Nagel, S. R. Random packings of frictionless particles. *Phys. Rev. Lett.* **88**, 075507 (2002).

[2] O'Hern, C. S., Silbert, L. E., Liu, A. J. & Nagel, S. R. Jamming at zero temperature and zero applied stress: The epitome of disorder. *Phys. Rev. E* **68**, 011306 (2003).

[3] Ramola, K. & Chakraborty, B. Stress Response of Granular Systems. *Journal of Statistical Physics* **169** (2017).

[4] Bitzek, E., Koskinen, P., Gähler, F., Moseler, M. & Gumbsch, P. Structural relaxation made simple. *Phys. Rev. Lett.* **97**, 170201 (2006).

[5] Guénolé, J. *et al.* Assessment and optimization of the fast inertial relaxation engine (fire) for energy minimization in atomistic simulations and its implementation in lammps *arXiv: 1908.02038* (2019).

[6] Plimpton, S. Fast parallel algorithms for short-range molecular dynamics. *Journal of Computational Physics* **117**, 1 (1995).

[7] Wang, Y., Hong, L., Wang, Y., Schirmacher, W. & Zhang, J. Disentangling boson peaks and van hove singularities in a model glass. *Phys. Rev. B* **98**, 174207 (2018).

[8] Majmudar, T. S. & Behringer, R. P. Contact force measurements and stress-induced anisotropy in granular materials. *Nature* **435**, 1079–1082 (2005).

[9] Bouchaud, J.-P. Granular media: some ideas from statistical physics. In Bouchaud, J., Barrat, J. L., Feigelman, M., Kurchan, J. & Dalibard, J. (eds.) *Slow Relaxations and Nonequilibrium Dynamics in Condensed Matter*, vol. 77, 185–202 (Les Ulis: EDP Sciences, 2003).

[10] Lemaître, A. Stress correlations in glasses. *Journal of Chemical Physics* **149**, 104107 (2018).

[11] DeGiuli, E. & McElwaine, J. Laws of granular solids: Geometry and topology. *Physical Review E - Statistical, Nonlinear, and Soft Matter Physics* **84** (2011).

[12] Prem, A., Vijay, S., Chou, Y. Z., Pretko, M. & Nandkishore, R. M. Pinch point singularities of tensor spin liquids. *Phys.Rev. B* **98**, 1 (2018).

[13] Otto, M., Bouchaud, J. P., Claudin, P. & Socolar, J. E. Anisotropy in granular media: Classical elasticity and directed-force chain network. *Phys. Rev. E* **67**, 24 (2003).

[14] Lantagne-Hurtubise, É., Bhattacharjee, S. & Moessner, R. Electric field control of emergent electrodynamics in quantum spin ice. *Physical Review B* **96**, 1–20 (2017).

[15] Xu, C. Gapless bosonic excitation without symmetry breaking: An algebraic spin liquid with soft gravitons. *Physical Review B - Condensed Matter and Materials Physics* **74**, 1–11 (2006).

[16] Henkes, S. & Chakraborty, B. Statistical mechanics framework for static granular matter. *Phys. Rev. E* **79**, 061301 (2009).

[17] Lois, G. *et al.* Stress correlations in granular materials: An entropic formulation. *Phys. Rev. E* **80**, 060303(R) (2009).

[18] DeGiuli, E. Edwards field theory for glasses and granular matter. *Phys. Rev. E* **98**, 33001 (2018).

[19] Ball, Robin C. & Blumenfeld, Raphael, Stress Field in Granular Systems: Loop Forces and Potential Formulation. *Physical Review Letters* **88**,115505 (2002).

[20] Pretko, M. Generalized electromagnetism of subdimensional particles: A spin liquid story. *Phys. Rev. B* **96**, 1–26 (2017).